NANO LETTERS

Letter

pubs.acs.org/NanoLett

Core/Shell Nanocomposites Produced by Superfast Sequential Microfluidic Nanoprecipitation

Dongfei Liu,[*,‡,†] Hongbo Zhang,[†,‡] Salvatore Cito,[†] Jin Fan,[§] Ermei Mäkilä,[∥] Jarno Salonen,[∥] Jouni Hirvonen,[†] Tiina M. Sikanen,[†] David A. Weitz,[‡] and Hélder A. Santos[*,†]

[†]Division of Pharmaceutical Chemistry and Technology, Drug Research Program, Faculty of Pharmacy, University of Helsinki, FI-00014 Helsinki, Finland

[‡]John A. Paulson School of Engineering and Applied Sciences, Harvard University, Cambridge, Massachusetts 02138, United States

[§]Department of Orthopaedics, The First Affiliated Hospital of Nanjing Medical University, 210029 Nanjing, China

[∥]Laboratory of Industrial Physics, Department of Physics and Astronomy, University of Turku, FI-20014 Turku, Finland

Supporting Information

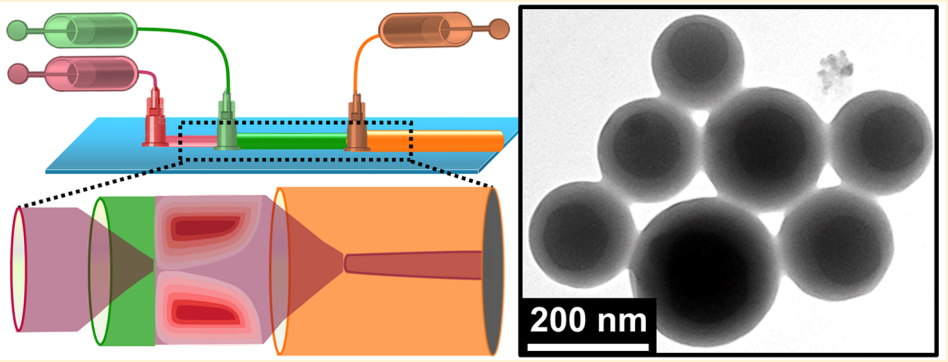

ABSTRACT: Although a number of techniques exist for generating structured organic nanocomposites, it is still challenging to fabricate them in a controllable, yet universal and scalable manner. In this work, a microfluidic platform, exploiting superfast (milliseconds) time intervals between sequential nanoprecipitation processes, has been developed for high-throughput production of structured core/shell nanocomposites. The extremely short time interval between the sequential nanoprecipitation processes, facilitated by the multiplexed microfluidic design, allows us to solve the instability issues of nanocomposite cores without using any stabilizers. Beyond high throughput production rate (~700 g/day on a single device), the generated core/shell nanocomposites harness the inherent ultrahigh drug loading degree and enhanced payload dissolution kinetics of drug nanocrystals and the controlled drug release from polymer-based nanoparticles.

KEYWORDS: *Sequential nanoprecipitation, superfast, core/shell, nanoparticles, stabilizer free*

Nanoparticles are of great scientific interest due to their wide varieties of potential applications in medical,[1] optical,[2,3] and electronic[4] fields. The synthesis approaches for nanoparticles can be generally classified into top-down and bottom-up. Top-down techniques, such as milling,[5,6] ultrasonication,[7] and high-pressure homogenization,[8] involve the size reduction of bulk materials to nanoscale. In this approach, high energy or pressure input is typically required, yet the efficiency of size reduction is limited, especially for nanoparticle sizes below 100 nm.[9] Moreover, fabrication of complex, structured, and multilayered nanocomposites by top-down approaches is technologically challenging. Conventional bottom-up techniques yield nanoparticles through chemical reactions,[10] nucleation,[11] or self-assembly.[12] The organic nanoparticles produced by such approaches are typically characterized by a wide size distribution, which can be ascribed to the alternation of synthesis conditions, as well as coagulation, aggregation, and agglomeration during particle growth.[13] Therefore, intensive formulation optimizations,[14] such as the case-specifically selection of stabilizers and adjustment of their concentrations, are indispensable for bottom-up approaches. These formulation optimizations ultimately impose constraints on the types of layered nanoparticles prepared by such approaches. For a core/shell structured organic nanocomposite prepared by the bottom-up approach, it is typically made in a two-step process: the formation of a nanoparticle core and then the encapsulation of nanoparticle core within a polymer nanomatrix. All intermediate steps, such as centrifugation, sonication, and vortexing, introduce significant variability in the characteristics of the formed core/shell nanocomposites.[15]

Received: August 3, 2016
Revised: December 2, 2016
Published: January 6, 2017

DOI: 10.1021/acs.nanolett.6b03251
Nano Lett. XXXX, XXX, XXX−XXX

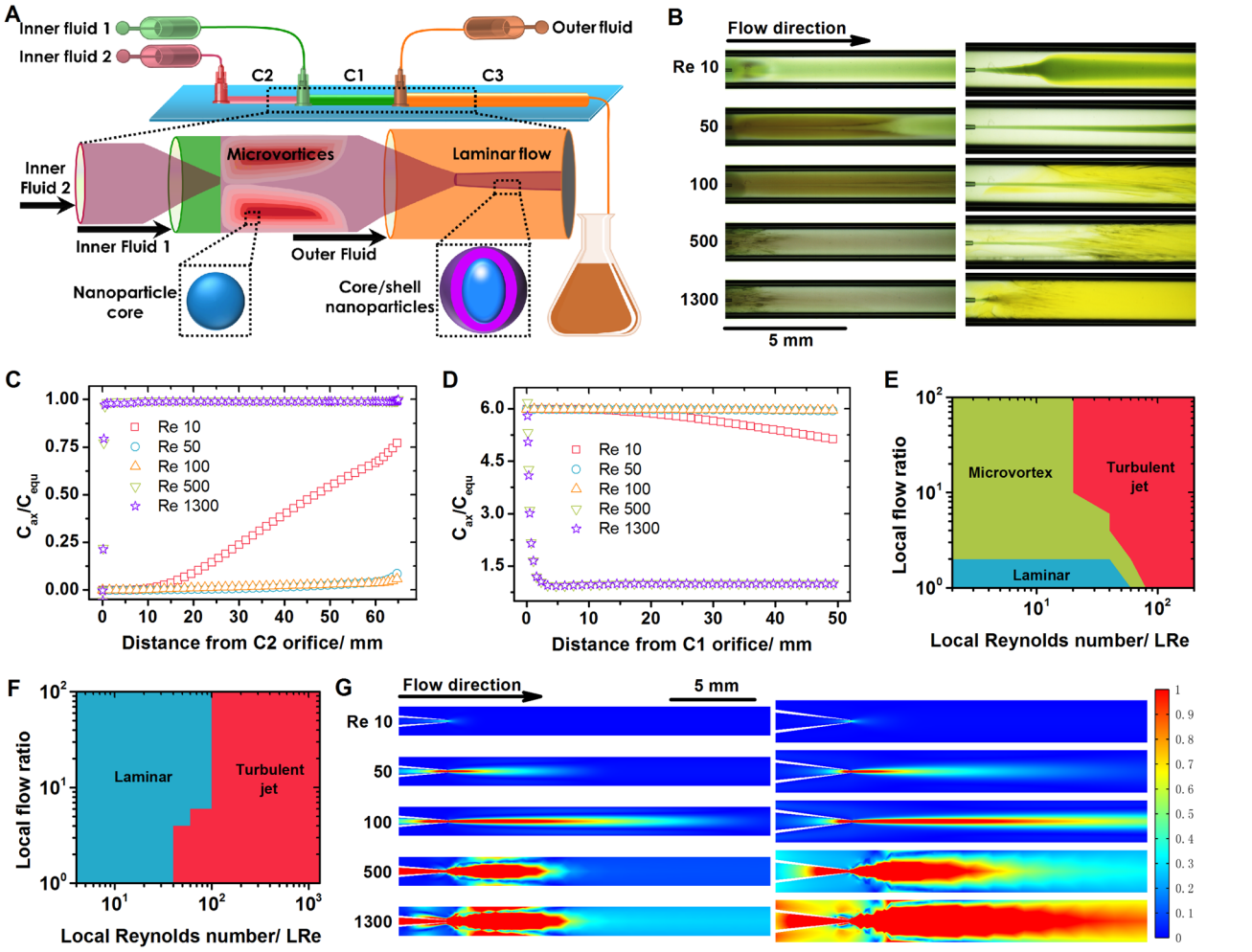

Figure 1. Superfast sequential nanoprecipitation microfluidic platform. (A) Overview and close-up of a 3D glass capillary device to prepare structured core/shell nanocomposites. (B) Fluid mixing patterns in the first (left side) and second (right side) mixing processes visualized by light microscope. (C and D) Plot of the ratios between the axial concentration (C_{ax}) and completely mixing equilibrated one (C_{equ}) at the first (C) and second (D) mixing processes. (E and F) Phase diagrams of flow regimes at the first (E) and second (F) mixing process. (G) Contour of the fluid velocities in the first (left side) and second (right side) mixing processes. The color bar on the right side represents the normalized velocity magnitude (0−1 m/s).

Microfluidics nanoprecipitation, one of the bottom-up techniques, has emerged for continuous production of a variety of nanomaterials by utilizing fluid diffusion, mixing, emulsification, or their combinations.[16] Benefiting from their small channel dimensions and the resulting large surface-to-volume ratio, microfluidic setups offer rapid and uniform mass transfer and consequently superior control over the characteristics of produced nanomaterials.[17] Liposomes,[18] polymer nanoparticles,[11] quantum dots,[19] iron oxide nanoparticles,[20] gold nanoparticles,[21] and gold nanorods[22] have been successfully prepared by the microfluidic approaches, showing smaller particle size and narrower size distribution than those prepared by the conventional bulk methods. Microfluidic nanoprecipitation is also an efficient approach toward the encapsulation of nanoparticles. Inorganic nanoparticles, such as porous silicon nanoparticles,[23] iron oxide nanoparticles,[24] gold nanoparticles,[24] and quantum dots,[24,25] have been efficiently encapsulated within the organic nanomatrix to synthesize the hybrid nanocomposites for biomedical applications. In terms of inorganic core/shell nanoparticles, an in situ redox process in microfluidic reactors has been developed to synthesize hybrid nanoparticles with amorphous metallic cores and uniform metal oxide shells at a large scale.[26]

Recently, a lipid−polymer hybrid nanoparticle, comprising a polymeric core to carry hydrophobic therapeutics and an outer lipid shell to prolong the circulation half-life, has been becoming a new class of nanocarrier for drug delivery applications.[15,27] The lipid−polymer hybrid nanoparticles combine the merits of the polymeric nanoparticles and liposomes. By varying the amounts of interfacial water between the polymer core and lipid shell, the rigidity of lipid−polymer hybrid nanoparticles can be tuned.[28,29] The obtained hard lipid−polymer hybrid nanoparticles demonstrated an enhanced anticancer efficacy than soft ones with the same amount of payload. Moreover, a hollow structured lipid−polymer hybrid nanoparticle has been prepared by a three-stage-mixing microfluidic device to efficiently entrap the hydrophilic therapeutics, such as small interfering RNA (siRNA).[30] The siRNA and doxorubicin coloaded hollow-structured rigid nanovesicle exhibits enhanced cancer treatment efficacy in a multidrug resistance tumor model.

The mass fraction of therapeutics (drug loading degree) is one of the most important features for particulate drug delivery

DOI: 10.1021/acs.nanolett.6b03251
Nano Lett. XXXX, XXX, XXX−XXX

systems. Although a variety of particles with distinguished characteristics have been successfully synthesized, the obtained carriers usually showed a low level of drug loading degrees. For example, the mass fractions of atorvastatin and dipeptidylpeptidase-4 were <1% in enteric hypromellose acetate succinate microparticles prepared by the droplet microfluidics.[31−33] When paclitaxel (PTX) was encapsulated in poly(lactic-*co*-glycolic acid) (PLGA) and acetalated dextran (AcDX),[34] the mass fraction of PTX in the microfluidic nanoprecipitated nanoparticles was only ∼6%,[11] although this value was significantly higher than those prepared by the bulk nanoprecipitation. In terms of microfluidic assembled docetaxel-loaded PLGA nanoparticles, the drug loading degree varied from ∼1% to ∼7%.[20,35,36] Because of the limited mass fraction of therapeutics, a large number of particles are unavoidable to be administrated to deliver a clinically relevant therapeutic dose. Consequently, the administrated large amount of nontherapeutic excipients may cause undesirable side effects.[37] When polymer nanoparticles were prepared by conventional methods, such as emulsion−solvent evaporation or polymer film hydration, the drug loading degree could achieve ∼27% and ∼15% for PTX[38,39] and sorafenib (SFN),[40] respectively. The PTX loading degree could reach up to 59% in poly(ethylene glycol)-*b*-PLGA nanomicelles,[41] after adjusting the hydrophobicity and hydrolytic lability of PTX by forming PTX−silicate conjugates. In comparison to the conventional emulsion−solvent evaporation or polymer film hydration methods, there is an urgent need to improve the drug loading degree of particles prepared by microfluidic approaches.

In this work, we present a new method for controlled of multilayered core/shell organic nanocomposites by multiplex microfluidics. Our microfluidic process is scalable and exploits sequential mixing of nanocomposite precursors with the corresponding nonsolvents to create superfast time intervals (in milliseconds range) between the sequential nanoprecipitation processes. In this manner, we can produce core/shell structured organic nanocomposites in a continuous process that is scalable to industrial production rate, with speed and easiness similar to production of single-material nanoparticles. Thanks to the short time interval between the repeated nanoprecipitation processes, we can overcome the instability of the nanocomposite cores, without any stabilizers, by simply encapsulating them in the nanomatrix (shell) immediately after the first precipitation process. This makes the presented approach universally applicable to production of a variety of nanocomposites, without the need of optimization of the stabilizer contents. When a drug nanocrystal has been encapsulated in the polymeric nanomatrix, the obtained core/shell organic nanocomposites harnessed the advantages of both polymeric nanoparticles, such as biodegradability and controlled drug release,[42] and those of drug nanocrystals, including the ultrahigh drug loading degree and enhanced dissolution rate.[43]

Our novel microfluidic platform that generates core/shell structured organic nanocomposites through a superfast sequential nanoprecipitation method is illustrated in Figure 1A. The microfluidic device consists of three sequentially nested cylindrical glass capillary tubes. In a general preparation process, the inner fluid 1 (F1, nanocomposite core and shell precursors) is pumped through the space between the two tapered capillaries 1 (C1) and 2 (C2), while the inner fluid 2 (F2, nonsolvent for the core precursor only) flows through the tapered C2. The outer fluid 3 (F3, nonsolvent for both core and shell precursors) is pumped through the space between C1 and capillary 3 (C3). The studied mass flow ratio among the F1, F2, and F3 is 1:5:30 unless otherwise specified. The specific flow rate of each fluid in terms of Reynolds number (Re, eq S1) has been listed in Table S1. All fluids flow in the same direction. By ensuring the small difference (∼0.1 mm) between the outer diameter of C2 and inner diameter of C1, as well as the outer diameter of C1 and inner diameter of C3, a coaxial geometry is achieved. Taking advantage of the coaxial geometry, this microfluidic device provides a distinct capability of rapid and uniform mass transfer.[44,45]

Fluid flow and mixing patterns of the device in terms of Re are visualized by adding bromophenol blue to F1 (Figure 1B). The bromophenol blue is used as a pH indicator; its color reversibly changes from blue at pH 4.6 to yellow at pH 3.0. Therefore, the color of fluids gradually became yellow upon mixing with the acidic F3 (pH 3). The highest Re achieved for this microfluidic device is 1300. This limit is constrained by the maximum force of the syringe pumps. Computational fluid dynamics (CFD) simulations are used to compute the concentration and velocity fields in the microfluidic domain. The CFD model is described by eqs S2−S4, and the finite element method has been implemented to solve the laminar flow when Re ≤ 100. At Re 10, a coaxial jet forms, and two microvortices generate beside the jet at the downstream of C2 nozzle in the first mixing process for both microscope imaging (Figure 1B) and CFD simulation (Figure S1). The bigger the Re, the larger the recirculation areas (microvortices). In the second mixing process, the F1 and F2 mixtures are focused by F3 at the downstream of C1 nozzle at Re 10 and 50, as shown in the microscope images and CFD simulation. The color of the F1 and F2 mixture flow changes to yellow farther in the downstream in CFD simulation, which can be attributed to the fluid diffusion between the F1 and F2 mixture and F3. Because of the fluid diffusion and decrease of the fluid pH conditions, a similar phenomenon was observed in microscope images. No complete mixing at the first and second mixing processes was detected within 50 mm downstream of C2 and C1 nozzles, which is confirmed by the nonconstant axial concentration (C_{ax}; Figure 1C and D).

By increasing flow rate, the flow regime in the first and second mixing process both transit to turbulent jet[20] at Re 500 and 1300. Therefore, the flow domain needs to be solved using direct numerical simulation (DNS) which requires an extremely fine mesh to solve the small-scale eddies. To overcome the computational limitation of using DNS, a turbulent flow model (eqs S5−S10) was employed to simulate the fluids mixing patterns at Re 500 and 1300. The coaxial jet disappears, and the uniform color of the fluids mixture at the downstream of C2 and C1 nozzles indicates the complete fluids mixing for both the first and second mixing process (Figures 1B and S1). C_{ax} reaches a plateau within 2 mm in the downstream of the nozzles (Figure 1C and D), further proving the complete mixing between the fluids. In CFD simulation, the later transition to turbulent flow than that in microscope imaging can be ascribed to oversized turbulent viscosity in the turbulence model which reduce the turbulence effect on mixing.[46]

The flow behavior is categorized into laminar, vortex, and turbulent jet regimes as summarized in Figure 1E and F. Local Re (LRe) and flow ratios in C1 and C3, respectively, were used to simplify the comparison. In the first mixing process, F2 is focused by F1 when the flow ratio between F2 and F1 (FR_{21}) is

DOI: 10.1021/acs.nanolett.6b03251
Nano Lett. XXXX, XXX, XXX−XXX

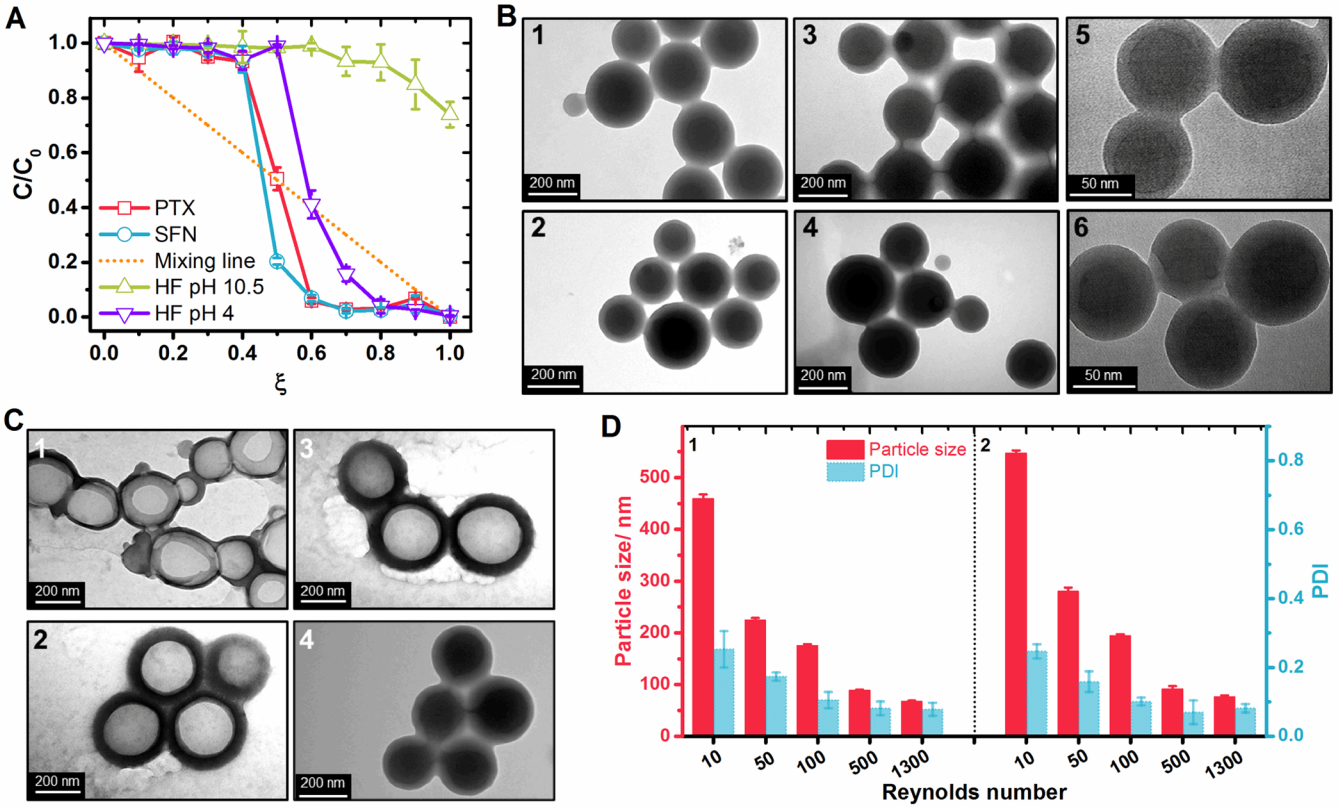

Figure 2. Superfast structured core/shell nanocomposites. (A) Solubility diagram of the nanocomposite precursors (n = 3). The straight short dot line connecting the solvent and nonsolvent is the mixing line. C and C_0 are the concentrations of nanocomposite precursors before and after adding nonsolvent, respectively. (B) TEM images of PTX@HF (1, 3 and 5) and SFN@HF (2, 4, and 6) prepared under different conditions. (1) and (2), Re 100 with a drug−polymer weight ratio of 1:1 in F1; (3) and (4), Re 100 with a drug−polymer weight ratio of 2:1 in F1; and (5) and (6), Re 1300 with a drug−polymer weight ratio of 1:1 in F1. (C) TEM images of PLGA@HF (1), PLGA@AcDX (2), PLGA@AcDXSP (3), and AcDXSP@HF (4). (D) Impact of Re on particle size and size distribution, obtained from dynamic light scattering, of PTX@HF (1) and SFN@HF (2) (n = 3).

close to 1. This regime transits to vortices and turbulence by increasing Re and FR_{21}. In the second mixing process, a laminar flow of the F1 and F2 mixture focused by F3 is observed when Re < 40. As Re gets bigger, the flow becomes unstable and changes to a turbulent jet regime in both mixing processes. The fluid mixing pattern transition is accelerated by accelerated the FR_{21} in the first mixing process. An opposite trend was observed in the second mixing process after boosting the flow ratio between F3 and mixture of F1 and F2.

As expected, the larger the Re, the higher the fluid velocity of this device (Figure 1G). The velocity of the fluids flowing through the capillary nozzles is much faster than that flowing in the rest space of the device, which can be attributed to the small dimension (~90 μm) of the nozzles. According to the flow rate and the mixing distance in the CFD simulation, extremely fast complete mixing (<0.5 ms) can be achieved for both the first and the second mixing at Re 500 and 1300, independent of the flow ratios. Our superfast sequential microfluidic nanoprecipitation platform enables fast fluids mixing on a small length scale at turbulence regime, as well as minimization of the device dimension.

To demonstrate the possible application of this microcapillary device, two poorly water-soluble anticancer drugs, PTX and SFN, and one enteric coating polymer hypromellose acetate succinate (H grade fine powders, HF; Figure S2) were selected to synthesize the drug nanocrystals encapsulated core/shell nanocomposites. Figure 2A outlines the solubility diagrams of nanocomposite precursors. We introduced the mixture fraction (ξ), which has the value ξ = 1 for the nonsolvent (water), and ξ = 0 for the solvent (acetone), to quantify the solubility of the nanocomposite precursors. When basic water (pH 10.5) served as the nonsolvent, the mixture fraction values at which the solubility limit crossed are approximately $\xi \approx 0.5$ for both PTX and SFN, and no solubility limit crossing has been observed for the HF. The solubility limit crossing mixture fraction value is $\xi \approx 0.6$ for HF by using acidic water (pH 3.0) as the nonsolvent. Once the solubility limit is crossed, diffusion controlled nucleation and aggregation of the drug and polymer molecules occur spontaneously, which can be ascribed to the poor solubility of these compounds in the nonsolvent.[47]

The precipitation process starts with supersaturation initiated by the diffusion and rapid mixing between the solvent and nonsolvent streams, driving the nucleation and precipitation of drug and polymers molecules sequentially. Specifically, drug nanocrystal cores formed at first by mixing a drug−acetone solution containing HF (F1) with a basic aqueous solution (pH 10.5, F2). Due to its pH-responsive feature, no precipitation of HF occurred at this stage. This drug nanocrystal suspension containing dissolved HF can then mix with another acidic aqueous solution (pH 4, F3). Because of the decreasing pH, the HF was precipitated and deposited onto the surface of firstly formed drug nanocrystals in the second mixing process.

We identified the structure and morphology of obtained nanocomposites by taking transmission (TEM) and scanning (SEM) electron microscope images. Clear core/shell structures

DOI: 10.1021/acs.nanolett.6b03251
Nano Lett. XXXX, XXX, XXX−XXX

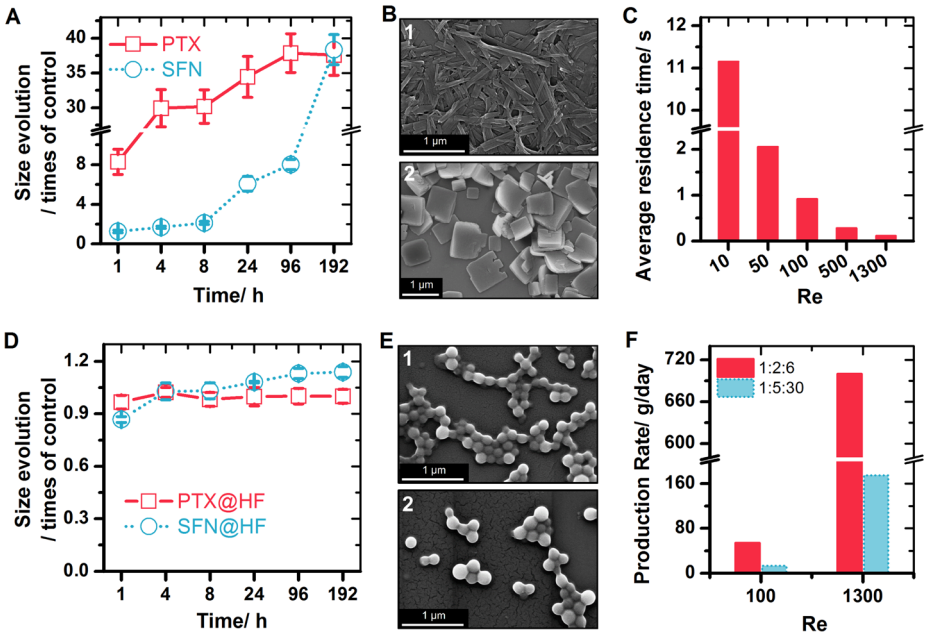

Figure 3. Stability of fabricated nanocomposites. (A) The size evolution of bare drug nanocrystals as a function of time (n = 3); the average size of freshly prepared nanoparticles served as the control. (B) SEM images of bare PTX (1) and SFN (2) particles after storing at 4 °C for 1 month. (C) The average residence time of drug nanocrystals in C1 in terms of Re. (D) The size evolution of drug nanocrystals encapsulated nanocomposites over time (n = 3); the average size of freshly prepared nanoparticles served as the control. (E) SEM images of PTX@HF (1) and SFN@HF (2) after storing at 4 °C for 1 month. (F) The SFN@HF production rate at Re 100 and 1300 with different flow ratios (1:2:6 and 1:5:30).

for both PTX and SFN nanocomposites (PTX@HF and SFN@HF) demonstrate the successful encapsulation of drug nanocrystals (Figure 2B). We checked the effect of the nanocomposite precursors ratio on the structure of the obtained nanocomposites at Re 100. The smaller is the polymer and drug weight ratio, the thinner is the polymer shell, independent of the types of drug nanocrystals encapsulated. When the drug−polymer weight ratio was 1:1, the sizes of drug nanocrystal cores and the whole core/shell nanocomposites decreased by simply increasing the Re from 100 to 1300. All the particles showed core/shell structures, indicating the high efficiency of this superfast sequential nanoprecipitation method. After encapsulation within the HF shell, the prepared nanocomposites were spherical in morphology (Figure S3). Both SEM and TEM images indicate that the polymer shells fully cover the surface of drug nanocrystals.

To demonstrate the versatility of our platform, different core/shell nanocomposites were fabricated (Figure 2C). The selection of poly(lactic-*co*-glycolic acid) (PLGA) to form the nanocomposite core is because of its higher brightness than other materials in TEM imaging (Figure S4), making the structure of generated nanomaterials easier to be identified. As expected, the obtained PLGA nanocomposites, PLGA@HF, presented a clearer core/shell structure than those of PTX@HF and SFN@HF. The negatively charged AcDX[34] and positively charged spermine-functionalized AcDX (AcDXSP)[48] were employed to encapsulate the PLGA cores (PLGA@AcDX and PLGA@AcDXSP). Regardless of the polymer charges, clear core/shell structures were always detected for both PLGA@AcDX and PLGA@AcDXSP. Moreover, our platform can also encapsulate the AcDXSP core within HF polymer nanomatrix to form core/shell structured AcDXSP@HF.

Next, we evaluated the impact of Re on the particle size and size distribution of PTX@HF and SFN@HF (Figure 2D). With Re > 10, the polydispersity index (PDI) was <0.2 for all the fabricated drug nanocrystals encapsulated nanocomposites, showing high size homogeneity. The microfluidic platform enables the superfast mixing of three fluids at higher Re and assembly of nanocomposite precursors sequentially. For both core/shell nanocomposites prepared, the higher the Re, the faster the mixing rate between fluids, and consequently, the smaller their average particle size and the narrower their size distribution.[25] By simply changing the Re, the reproducibility of the core/shell nanocomposites was controlled in the range of 60−450 nm and 70−550 nm for PTX@HF and SFN@HF, respectively. This microfluidics platform offers a good control of preparation process, leading to tunable particle size with narrow size distribution.[17,49] The average particle size obtained from dynamic light scattering is in accordance to the size of separated nanocomposites showed in the TEM and SEM images. As shown in Figure S5, the solid bridges among the nanocomposites disappeared after 5 times diluting of the suspension. According to the dynamic light scattering results and EM images of diluted suspensions, the solid bridge forming among the nanocomposites can be attributed to the drying process. To show more representative nanocomposites, we still chose the nanocomposites with relatively high concentrations for SEM and TEM imaging. With regard to the reproducible nanocomposites synthesis, PTX@HF and SFN@HF with the desired particle size and narrow size distribution were obtained in over 20 independent nanoprecipitation experiments at Re 50 and 500 (Figure S6). The operation of this microfluidic platform in a continuous mode offers a high batch-to-batch reproducibility for fabricated nanomaterials.

The freshly produced bare PTX and SFN particles were in nanoscale; however, their size increased ~37 times after 192 h (Figure 3A). The size evolution rate of SFN particles was slower than that of PTX. As shown in Figure 3B, the precipitation of bare PTX yielded several micrometer long rods, whereas flat trapezoids of several micrometer wide formed

DOI: 10.1021/acs.nanolett.6b03251
Nano Lett. XXXX, XXX, XXX−XXX

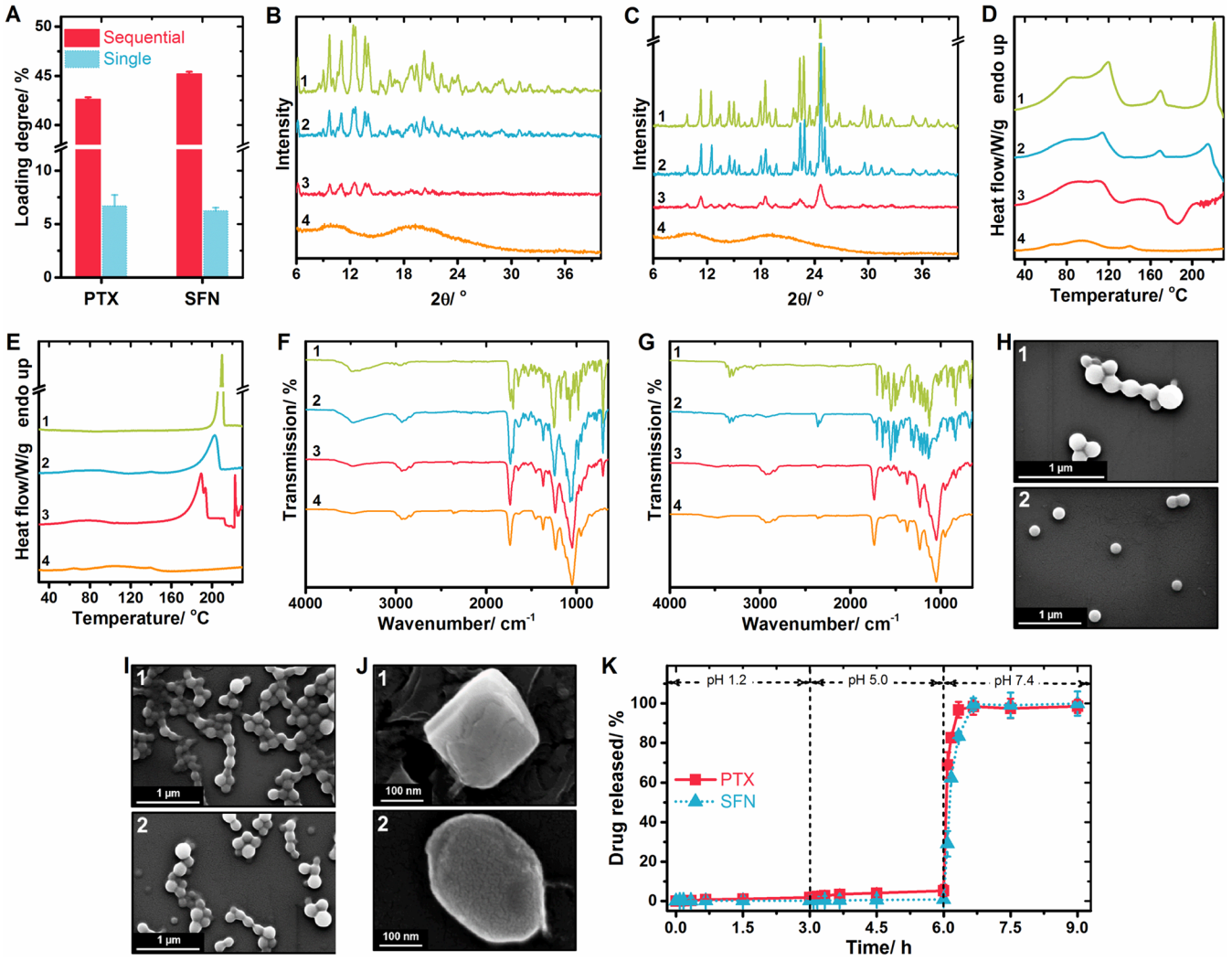

Figure 4. Physicochemical characterization of fabricated nanocomposites. (A) Drug loading degrees of PTX and SFN loaded nanomaterials fabricated by either single or sequential nanoprecipitations (n = 10). (B) X-ray powder diffractogram of PTX (1), PTX-HF PM (2), PTX@HF (3), and HF (4). (C) Diffractogram of SFN (1), SFN-HF PM (2), SFN@HF (3), and HF (4). (D) DSC curve of PTX (1), PTX-HF PM (2), PTX@HF (3), and HF (4). (E) DSC curve of SFN (1), SFN-HF PM (2), SFN@HF (3), and HF (4). (F) FTIR spectrum of PTX (1), PTX-HF PM (2), PTX@HF (3), and HF (4). (G) FTIR spectrum of SFN (1), SFN-HF PM (2), SFN@HF (3), and HF (4). (H–J) The SEM images of PTX@HF (1) and SFN@HF (2) after incubating with a buffer solution of pH 1.2 (H), pH 5.0 (I), and pH 7.4 (J) for 10 min. (K) Drug release profiles of prepared core/shell nanocomposites with continuous changes in the pH conditions starting from pH 1.2 to 7.4 at 37 °C (n = 3).

for the bare SFN particles. Similar evolution trends on the PDI of PTX and SFN particles were observed (Figure S7). The small increasing times on the PDI for PTX can be ascribed to its fast particle size evolution, leading to a large PDI for the control sample. Due to coagulation, aggregation, or agglomeration, the size of the obtained drug particles further grew,[50] making the size retaining of drug particles prepared by bottom-up approaches.[51,52] The Ostwald ripening, the growth of bigger particles in expense of the smaller ones, is another important explanation for the increasing average particle size of bare drug nanocrystals.[51,52]

We argue that the polymer shells can immediately cover the surface of freshly formed drug nanocrystals in this superfast sequential nanoprecipitation method, which can address the size stability issue for drug nanocrystals synthesized by bottom-up approaches. We measured the residence time distribution (RTD, eqs S11–S14) of drug nanocrystals inside C1 (Figure S8). In this microfluidic device, the higher the Re, the shorter the average residence time of drug nanocrystals in C1 (Figure 3C). We consider the time spent for drug nanocrystals to pass through C1 as the time intervals between the first and second nanoprecipitation. The time interval between the two precipitations can be tuned from over 10 s at Re 10 to less than 0.1 s at Re 1300. The rapid process between two nanoprecipitation processes enable the superfast deposition of HF to cover the surfaces of freshly formed drug nanocrystals. When the amount of HF deposited onto drug nanocrystals increases sufficiently, the growth of drug nanocrystals are stabilized. Benefiting from the superfast formation of polymer shells, we can prepare drug nanocrystals encapsulated core/shell structured nanocomposites without using any stabilizers and easily keep their size below 100 nm. No significant changes on the average particle size (Figure 3D), particle size distribution (Figure S7), and particle morphology (Figure 3E) were observed for PTX@HF and SFN@HF after one-month storage at 4 °C.

Since the residence time of drug nanocrystals in the alkaline condition is extremely short and the final pH value of the

DOI: 10.1021/acs.nanolett.6b03251
Nano Lett. XXXX, XXX, XXX–XXX

nanosuspension is close to neutral, the loaded therapeutics are expected to be stable. The chromatograms of loaded therapeutics obtained by reversed-phase high-performance liquid chromatography (HPLC) are presented in Figure S9. The symmetric and sharp chromatographic peaks of PTX and SFN indicate the good stability of loaded therapeutics during the core/shell nanocomposite preparation process.

One major concern for the synthesis of nanomaterials using microfluidic platforms is their productivity.[27,36] We assume that all of the precursors pumped into the microfluidic platform can be converted into the core/shell nanocomposites. High flow rates of this microfluidic device offer an inherently high throughput with superfast nanocomposite production. When the concentrations of SFN and HF were respectively fixed at 25 mg/mL with a flow ratio of 1:2:6 (F1:F2:F3), the production rate of the nanocomposites can reach ~700 g/day at Re 1300 (Figure 3F and Table S2). The single microfluidic device can meet the nanomaterials production rate requirements for both the clinical studies (0.1 kg/day) and industrial-scale production (1 kg/day).[20]

Most drug-loaded nanoparticles are composed primarily of nontherapeutic hosting components. For instance, the PTX and SFN loading degree (mass fraction of therapeutics in nanoparticles) was only ~6% for the drug loaded HF nanoparticles prepared by the single microfluidic nanoprecipitation method (Figure 4A).[11] Consequently, a large amount of nanocarriers are needed to deliver a clinically relevant therapeutic dose, which may cause undesirable side effects and drive up the treatment cost.[37] The simultaneous nanoprecipitation of nanoparticle precursors and therapeutic molecules limits the space inside the polymer matrix to incorporate therapeutics. In the core/shell nanocomposites generated by the superfast sequential nanoprecipitation method, the encapsulated drug nanocrystal takes the major part of the obtained nanocomposite; therefore, ultrahigh drug loading degree can be achieved. Specifically, the PTX loading degree increased from ~6.7% to 42.6% and from 6.2% to 45.2% for SFN after using the superfast sequential nanoprecipitation method with a polymer−drug ratio of 1:1 in F1 (Figure 4A). The reproducible syntheses of core/shell nanocomposites with desired drug loading degrees were obtained with respect to PTX@HF and SFN@HF in 10 independent experiments, showing good batch-to-batch reproducibility.

Because amorphous materials are generally unstable, cohesive, potentially hygroscopic, and prone to recrystallization, the ideal drug nanoparticle cores for long-term storage should be in crystalline form.[9] We confirmed the solid state of the payloads in the core/shell nanocomposites by X-ray diffraction (XRD; Figures 4B and C) and differential scanning calorimetry (DSC; Figures 4D and E). The XRD diffractograms of the PTX-HF physical mixture (PTX-HF PM) and PTX@HF show that the samples appear to have retained their crystallinity. While the PTX@HF did not present a melting endotherm, the dehydration of the PTX crystals in the encapsulated sample was clearly observable confirming the XRD observations. Similar XRD profiles were also identified between the SFN and HF physical mixture (SFN-HF PM) and SFN@HF, in which SFN was in crystal form. This was also confirmed by the DSC results, showing the SFN to have retained its crystallinity in SFN@HF, although its melting temperature was clearly reduced due to the small size of the nanocomposites (Table S3). The PTX@HF and SFN@HF nanocompoistes were further characterized by the Fourier transformed infrared spectroscopy (FTIR) using a horizontal attenuated total reflectance (ATR) accessory. The FTIR spectra of PTX-HF PM and PTX@HF showed the characteristic bands from HF and PTX (Figure 4F). The characteristic bands of PTX in the FTIR spectrum of PTX@HF were weaker than those of PTX-HF PM, although they have similar PTX-HF weight ratios. When looking at the FTIR spectrum of SFN@HF, the SFN characteristic bands almost disappeared (Figure 4G). The weaker characteristic bands of payloads for both PTX@HF and SFN@HF can be ascribed to their core/shell structure and the encapsulation of drug nanocrystals within the HF matrix.

Next, we investigated the morphological changes and drug release kinetics of the obtained core/shell nanocomposites at different pH conditions, which can provide information on the integrity of the polymer shells. All nanomaterials, PTX@HF, SFN@HF, and HF nanoparticles, maintained their structure at pH 1.2 and 5.0 (Figures 4H, I and S10). As a result of the polymer dissolution, the bare HF nanoparticles became smaller and eventually disappeared at pH 7.4 (Figure S10). After the HF dissolution, the exposure of the drug nanocrystals was observed for both PTX@HF and SFN@HF (Figure 4J). Owing to their low aqueous solubility, fetal bovine serum (FBS; 10%, v/v) was added into the release medium to solubilize PTX and SFN. Because of its poor aqueous solubility, no drug was released from the SFN bulk powders at pH 1.2, 5.0, and 7.4 (Figure S11). Slow drug dissolution kinetics (<20% within 6 h) was detected for the PTX bulk powders at all three tested pH values. Independent on the pH conditions of the release media tested, both bare PTX and SFN nanocrystals reached complete drug release within 5 min (Figure S12). Barely no drug (<7%) was released from the PTX@HF and SFN@HF at pH 1.2 and 5.0 (Figures 4K and S13), allowing us to conclude that both PTX and SFN nanocrystals have been tightly entrapped inside the HF polymer shell. Regardless of the loaded drugs, both core/shell nanocomposites showed similar complete drug release profiles after increasing the pH value to 7.4 (Figures 4K and S13), which can be ascribed to the dissolution of HF and the exposure of the encapsulated drug nanocrystals. In comparison to bulk drug powders, the dissolution kinetics was enhanced for the bare drug nanocrystals at all three pH conditions and the core/shell structured nanocomposites at pH 7.4, benefiting from their nanoscale particle size and high surface area. Overall, the drug release kinetics together with the particle morphology at different pH conditions confirmed the full surface coverage of drug nanocrystals within the HF shells.

In conclusion, we have developed a superfast sequential microfluidic nanoprecipitation platform, through which core/shell structured nanocomposites can be efficiently synthesized at a super high speed in one continuous process. The short time interval between the sequential nanoprecipitation processes enables the preparation of core/shell nanocomposites without using any stabilizers and also improves the stability of the encapsulated cargos. The operation of this microfluidic platform in a continuous mode offers a high batch-to-batch reproducibility and high throughput production of drug nanocrystal encapsulated nanocomposites at rates up to 700 g/day on a single device. The superfast mixing of fluids at high Re results in a homogeneous size distribution of core/shell nanocomposites. Furthermore, the obtained nanocomposites with drug nanocrystal cores combine the controlled drug release feature of the polymer nanoparticles and the ultrahigh drug loading degree and enhanced therapeutic dissolution

DOI: 10.1021/acs.nanolett.6b03251
Nano Lett. XXXX, XXX, XXX−XXX

kinetics of the drug nanocrystals, showing its great potential in drug delivery applications.

■ ASSOCIATED CONTENT

Supporting Information

The Supporting Information is available free of charge on the ACS Publications website at DOI: 10.1021/acs.nanolett.6b03251.

Experimental details, supporting tables, distribution of normalized concentration of nanocomposite precursors, structure of hypromellose acetate succinate, additional characterizations, and RTD curves (PDF)

■ AUTHOR INFORMATION

Corresponding Authors

*E-mail: dongfei.liu@helsinki.fi.
*E-mail: helder.santos@helsinki.fi.

ORCID

Ermei Mäkilä: 0000-0002-8300-6533
Jarno Salonen: 0000-0002-5245-742X
Tiina M. Sikanen: 0000-0002-0788-1301
Hélder A. Santos: 0000-0001-7850-6309

Author Contributions

D.L. and H.A.S. conceived the idea and designed the experiments. D.L. conducted the experiments. H.Z. took the SEM images. D.L., S.C., J.F., and T.M.S. performed the CFD simulation and RTD calculation. E.M. and J.S. conducted the solid state analysis. All the authors contributed to the design and analysis of the experiments, and revision and commenting of the paper.

Notes

The authors declare no competing financial interest.

■ ACKNOWLEDGMENTS

We acknowledge financial support from the Academy of Finland (Grants No. 252215 and 281300), the University of Helsinki Research Funds, the Biocentrum Helsinki, the European Research Council (Grants No. 310892 and 311705), the Jane and Aatos Erkko Foundation (Grants No. 4704010 and 4704482), and the National Natural Science Foundation of China (Grant No. 81401807). We thank the Electron Microscopy Unit of the Institute of Biotechnology, University of Helsinki, for providing laboratory facilities for TEM imaging. A patent application was submitted to cover the microfluidic device and the production of core/shell nanocomposites.

■ REFERENCES

(1) Langer, R. *Nature* **1998**, *392*, 5−10.
(2) Alivisatos, A. P. *Science* **1996**, *271*, 933−937.
(3) Lal, S.; Link, S.; Halas, N. J. *Nat. Photonics* **2007**, *1*, 641−648.
(4) Grieve, K.; Mulvaney, P.; Grieser, F. *Curr. Opin. Colloid Interface Sci.* **2000**, *5*, 168−172.
(5) Tjerkstra, R. W.; Segerink, F. B.; Kelly, J. J.; Vos, W. L. *J. Vac. Sci. Technol. B* **2008**, *26*, 973−977.
(6) Van Eerdenbrugh, B.; Van den Mooter, G.; Augustijns, P. *Int. J. Pharm.* **2008**, *364*, 64−75.
(7) Zhao, H. P.; Feng, X. Q.; Gao, H. J. *Appl. Phys. Lett.* **2007**, *90*, 073112.
(8) Keck, C. M.; Muller, R. H. *Eur. J. Pharm. Biopharm.* **2006**, *62*, 3−16.
(9) Chan, H. K.; Kwok, P. C. L. *Adv. Drug Delivery Rev.* **2011**, *63*, 406−416.
(10) Sun, S. H.; Murray, C. B.; Weller, D.; Folks, L.; Moser, A. *Science* **2000**, *287*, 1989−1992.
(11) Liu, D. F.; Cito, S.; Zhang, Y. Z.; Wang, C. F.; Sikanen, T. M.; Santos, H. A. *Adv. Mater.* **2015**, *27*, 2298−2304.
(12) Kalsin, A. M.; Fialkowski, M.; Paszewski, M.; Smoukov, S. K.; Bishop, K. J. M.; Grzybowski, B. A. *Science* **2006**, *312*, 420−424.
(13) Kaufman, J. J.; Tao, G. M.; Shabahang, S.; Banaei, E. H.; Deng, D. S. S.; Liang, X. D.; Johnson, S. G.; Fink, Y.; Abouraddy, A. F. *Nature* **2012**, *487*, 463−467.
(14) D'Addio, S. M.; Prud'homme, R. K. *Adv. Drug Delivery Rev.* **2011**, *63*, 417−426.
(15) Zhang, L.; Chan, J. M.; Gu, F. X.; Rhee, J. W.; Wang, A. Z.; Radovic-Moreno, A. F.; Alexis, F.; Langer, R.; Farokhzad, O. C. *ACS Nano* **2008**, *2*, 1696−1702.
(16) Feng, Q.; Sun, J.; Jiang, X. *Nanoscale* **2016**, *8*, 12430−12443.
(17) Valencia, P. M.; Farokhzad, O. C.; Karnik, R.; Langer, R. *Nat. Nanotechnol.* **2012**, *7*, 623−629.
(18) Jahn, A.; Vreeland, W. N.; DeVoe, D. L.; Locascio, L. E.; Gaitan, M. *Langmuir* **2007**, *23*, 6289−6293.
(19) Shestopalov, I.; Tice, J. D.; Ismagilov, R. F. *Lab Chip* **2004**, *4*, 316−321.
(20) Lim, J. M.; Swami, A.; Gilson, L. M.; Chopra, S.; Choi, S.; Wu, J.; Langer, R.; Karnik, R.; Farokhzad, O. C. *ACS Nano* **2014**, *8*, 6056−6065.
(21) Cabeza, V. S.; Kuhn, S.; Kulkarni, A. A.; Jensen, K. F. *Langmuir* **2012**, *28*, 7007−7013.
(22) Lohse, S. E.; Eller, J. R.; Sivapalan, S. T.; Plews, M. R.; Murphy, C. J. *ACS Nano* **2013**, *7*, 4135−4150.
(23) Liu, D. F.; Zhang, H. B.; Mäkilä, E.; Fan, J.; Herranz-Blanco, B.; Wang, C. F.; Rosa, R.; Ribeiro, A. J.; Salonen, J.; Hirvonen, J.; Santos, H. A. *Biomaterials* **2015**, *39*, 249−259.
(24) Kim, Y.; Fay, F.; Cormode, D. P.; Sanchez-Gaytan, B. L.; Tang, J.; Hennessy, E. J.; Ma, M. M.; Moore, K.; Farokhzad, O. C.; Fisher, E. A.; Mulder, W. J. M.; Langer, R.; Fayad, Z. A. *ACS Nano* **2013**, *7*, 9975−9983.
(25) Valencia, P. M.; Basto, P. A.; Zhang, L.; Rhee, M.; Langer, R.; Farokhzad, O. C.; Karnik, R. *ACS Nano* **2010**, *4*, 1671−1679.
(26) Song, Y. J.; Ji, S. X.; Song, Y. J.; Li, R. S.; Ding, J.; Shen, X. M.; Wang, R. M.; Xu, R. W.; Gu, X. Y. *J. Phys. Chem. C* **2013**, *117*, 17274−17284.
(27) Kim, Y. T.; Chung, B. L.; Ma, M. M.; Mulder, W. J. M.; Fayad, Z. A.; Farokhzad, O. C.; Langer, R. *Nano Lett.* **2012**, *12*, 3587−3591.
(28) Zhang, L.; Feng, Q.; Wang, J.; Zhang, S.; Ding, B.; Wei, Y.; Dong, M.; Ryu, J. Y.; Yoon, T. Y.; Shi, X.; Sun, J.; Jiang, X. *ACS Nano* **2015**, *9*, 9912−9921.
(29) Sun, J.; Zhang, L.; Wang, J.; Feng, Q.; Liu, D.; Yin, Q.; Xu, D.; Wei, Y.; Ding, B.; Shi, X.; Jiang, X. *Adv. Mater.* **2015**, *27*, 1402−1407.
(30) Zhang, L.; Feng, Q.; Wang, J. L.; Sun, J. S.; Shi, X. H.; Jiang, X. Y. *Angew. Chem., Int. Ed.* **2015**, *54*, 3952−3956.
(31) Liu, D.; Zhang, H.; Herranz-Blanco, B.; Mäkilä, E.; Lehto, V. P.; Salonen, J.; Hirvonen, J.; Santos, H. A. *Small* **2014**, *10*, 2029−2038.
(32) Li, W.; Liu, D.; Zhang, H.; Correia, A.; Mäkilä, E.; Salonen, J.; Hirvonen, J.; Santos, H. A. *Acta Biomater.* **2016**, DOI: 10.1016/j.actbio.2016.10.042.
(33) Araújo, F.; Shrestha, N.; Shahbazi, M. A.; Liu, D.; Herranz-Blanco, B.; Mäkilä, E. M.; Salonen, J. J.; Hirvonen, J. T.; Granja, P. L.; Sarmento, B.; Santos, H. A. *ACS Nano* **2015**, *9*, 8291−302.
(34) Broaders, K. E.; Cohen, J. A.; Beaudette, T. T.; Bachelder, E. M.; Frechet, J. M. J. *Proc. Natl. Acad. Sci. U. S. A.* **2009**, *106*, 5497−5502.
(35) Kolishetti, N.; Dhar, S.; Valencia, P. M.; Lin, L. Q.; Karnik, R.; Lippard, S. J.; Langer, R.; Farokhzad, O. C. *Proc. Natl. Acad. Sci. U. S. A.* **2010**, *107*, 17939−17944.
(36) Karnik, R.; Gu, F.; Basto, P.; Cannizzaro, C.; Dean, L.; Kyei-Manu, W.; Langer, R.; Farokhzad, O. C. *Nano Lett.* **2008**, *8*, 2906−2912.
(37) Della Rocca, J.; Liu, D. M.; Lin, W. B. *Nanomedicine* **2012**, *7*, 303−305.

DOI: 10.1021/acs.nanolett.6b03251
Nano Lett. XXXX, XXX, XXX−XXX

(38) Lim, H. J.; Nam, H. Y.; Lee, B. H.; Kim, D. J.; Ko, J. Y.; Park, J. S. *Biotechnol. Prog.* **2007**, *23*, 693−697.
(39) Wang, C.; Wang, Y. J.; Wang, Y. J.; Fan, M.; Luo, F.; Qian, Z. Y. *Int. J. Pharm.* **2011**, *414*, 251−259.
(40) Park, W.; Chen, J.; Cho, S.; Park, S. J.; Larson, A. C.; Na, K.; Kim, D. H. *ACS Appl. Mater. Interfaces* **2016**, *8*, 12711−12719.
(41) Han, J.; Michel, A. R.; Lee, H. S.; Kalscheuer, S.; Wohl, A.; Hoye, T. R.; McCormick, A. V.; Panyam, J.; Macosko, C. W. *Mol. Pharmaceutics* **2015**, *12*, 4329−4335.
(42) Soppimath, K. S.; Aminabhavi, T. M.; Kulkarni, A. R.; Rudzinski, W. E. *J. Controlled Release* **2001**, *70*, 1−20.
(43) Fuhrmann, K.; Gauthier, M. A.; Leroux, J. C. *Mol. Pharmaceutics* **2014**, *11*, 1762−1771.
(44) Othman, R.; Vladisavljevic, G. T.; Bandulasena, H. C. H.; Nagy, Z. K. *Chem. Eng. J.* **2015**, *280*, 316−329.
(45) Rhee, M.; Valencia, P. M.; Rodriguez, M. I.; Langer, R.; Farokhzad, O. C.; Karnik, R. *Adv. Mater.* **2011**, *23*, H79−H83.
(46) Hershey, D. E.; Thomas, B. G.; Najjar, F. M. *Int. J. Numer. Methods Fluids* **1993**, *17*, 23−47.
(47) Cheng, J. C.; Vigil, R. D.; Fox, R. O. *J. Colloid Interface Sci.* **2010**, *351*, 330−342.
(48) Cohen, J. L.; Schubert, S.; Wich, P. R.; Cui, L.; Cohen, J. A.; Mynar, J. L.; Frechet, J. M. J. *Bioconjugate Chem.* **2011**, *22*, 1056−1065.
(49) Whitesides, G. M. *Nature* **2006**, *442*, 368−373.
(50) Sinha, B.; Muller, R. H.; Moschwitzer, J. P. *Int. J. Pharm.* **2013**, *453*, 126−141.
(51) Hu, J.; Ng, W. K.; Dong, Y. C.; Shen, S. C.; Tan, R. B. H. *Int. J. Pharm.* **2011**, *404*, 198−204.
(52) Sun, B.; Yeo, Y. *Curr. Opin. Solid State Mater. Sci.* **2012**, *16*, 295−301.

DOI: 10.1021/acs.nanolett.6b03251
Nano Lett. XXXX, XXX, XXX−XXX